

# We are IntechOpen, the world's leading publisher of Open Access books Built by scientists, for scientists

4,800

Open access books available

122,000

International authors and editors

135M

Downloads

Our authors are among the

154

Countries delivered to

TOP 1%

most cited scientists

12.2%

Contributors from top 500 universities



WEB OF SCIENCE™

Selection of our books indexed in the Book Citation Index  
in Web of Science™ Core Collection (BKCI)

Interested in publishing with us?  
Contact [book.department@intechopen.com](mailto:book.department@intechopen.com)

Numbers displayed above are based on latest data collected.  
For more information visit [www.intechopen.com](http://www.intechopen.com)



# Cavity Generation Modeling of Fiber Fuse in Single-Mode Optical Fibers

Yoshito Shuto

## Abstract

The evolution of a fiber fuse in a single-mode optical fiber was studied theoretically. To clarify both the silica-glass densification and cavity formation, which are observed in fiber fuse propagation, we investigated a nonlinear oscillation model using the Van der Pol equation. This model was able to phenomenologically explain the densification of the core material, the formation of periodic cavities, the cavity shape, and the regularity of the cavity pattern in the core layer as a result of the relaxation oscillation and cavity compression and/or deformation. Furthermore, the production and diffusion of O<sub>2</sub> gas in the high-temperature core layer were described on the basis of the nonlinear oscillation model.

**Keywords:** fiber fuse, nonlinear oscillation, Van der Pol equation

## 1. Introduction

Owing to the progress of dense wavelength-division multiplexing (DWDM) technology using an optical-fiber amplifier, we can exchange large amounts of data at a rate of over 100 Tbit/s over several hundred kilometers [1]. However, it is widely recognized that the maximum transmission capacity of a single strand of fiber is rapidly approaching its limit of  $\sim 100$  Tbit/s owing to the optical power limitations imposed by the fiber fuse phenomenon and the finite transmission bandwidth determined by optical-fiber amplifiers [2]. To overcome these limitations, space-division multiplexing (SDM) technology using a multicore fiber (MCF) was proposed [3, 4], and 1 Pbit/s transmission was demonstrated using a low-crosstalk 12-core fiber [5].

The fiber fuse phenomenon was first observed in 1987 by British scientists [6–9]. Several review articles [10–14] have been recently published that cover many aspects of the current understanding of fiber fuses.

A fiber fuse can be generated by bringing the end of a fiber into contact with an absorbent material or melting a small region of a fiber using an arc discharge of a fusion splice machine [6, 15–17]. If a fiber fuse is generated, an intense blue-white flash occurs in the fiber core, and this flash propagates along the core in the direction of the optical power source at a velocity on the order of 1 m/s. The temperature and pressure in the region where this flash occurs have been estimated to be about  $10^4$  K and  $10^4$  atm, respectively [18]. Fuses are terminated by gradually

reducing the laser power to a termination threshold at which the energy balance in the fuse is broken.

The critical diameter  $d_{melted}$ , which is usually larger than the core diameter  $2r_c$ , is a characteristic dimensional parameter of the fiber fuse effect. In the inner area with diameter  $d \leq d_{melted}$ , a fiber fuse (high-temperature ionized gas plasma) propagates and silica glass is melted [18].  $d_{melted}$ , defined as the diameter of the melting area, is considered as the radial size of the plasma generated in the fiber fuse [19]. Dianov *et al.* reported that the refractive index of the inner area with  $d \leq d_{melted}$  in Ge-doped and/or pure silica core fibers is increased by silica-glass densification and/or the redistribution of the dopant (Ge) [20].

When a fiber fuse is generated, the core layer in which the fuse propagates is seriously damaged, and the damage has the form of periodic bullet-shaped cavities or non-periodic filaments remaining in the core [6–9, 16–32] (see **Figure 1**). Needless to say, the density in a cavity or filament is lower than that of the neighboring silica glass. It has been found that molecular oxygen is released and remains in the cavities while maintaining a high pressure (about 4 atm [7] or 5–10 atm [20]) at room temperature. Recently, several types of sensors based on periodic cavities have been proposed as a cost-effective approach to sensor production [27–29].

The dynamics of cavity formation have been investigated since the discovery of the fiber fuse phenomenon. Dianov and coworkers observed the formation of periodic bullet-shaped cavities 20–70  $\mu\text{s}$  after the passage of a plasma leading edge [30, 31].

Kashyap reported that the cavity shape was dependent on the nature of the input laser light (CW or pulses) operated at a wavelength  $\lambda_0$  of 1.064  $\mu\text{m}$  when the average input power was maintained at 2 W [7, 15]. When CW light was input, the cavities appeared to be elliptical and cylindrically symmetric. On the other hand, short asymmetric cavities were formed by injecting (mode-locked) pulses with 100 ps FWHM (full width at half maximum), while long bullet-shaped cavities were observed by injecting pulses with 190 ps FWHM [7, 15]. Hand and Russell reported the appearance of highly regular periodic damage tracks in germanosilicate fibers at  $\lambda_0 = 488$  and 514 nm [9]. Davis *et al.* reported that long non-periodic filaments occurred in germanium-doped depressed clad fibers, and a periodic damage pattern was observed in fibers doped with phosphorus and germanium at  $\lambda_0 = 1.064 \mu\text{m}$  [21, 22]. Atkins *et al.* observed both periodic and long non-periodic damage tracks created in a germanosilicate-core single-mode fiber transmitting about 2 W of power at 488 nm [32]. Dianov and coworkers reported the formation of periodic damage in a silica-core fiber at 1.064 and 1.21  $\mu\text{m}$  [18, 30, 31] and long non-periodic damage in a germanosilicate silica core fiber at 488 and 514 nm [20].

Todoroki classified fiber fuse propagation into three modes (unstable, unimodal, and cylindrical) according to the plasma volume relative to the pump beam size [26]. When the pump power was increased or decreased rapidly, an increase in the

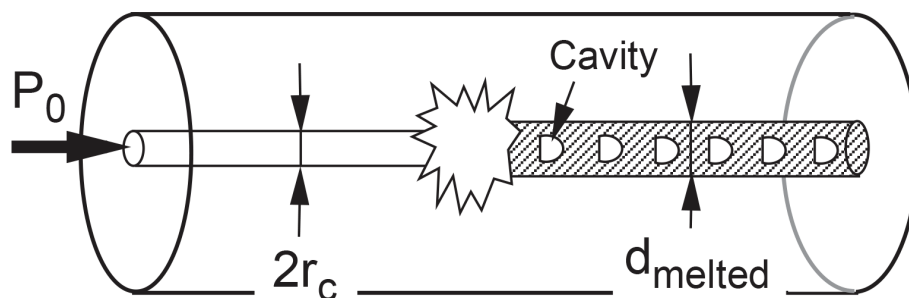


**Figure 1.**  
Schematic view of damaged optical fiber.

length of the void-free segment or the occurrence of an irregular void pattern was observed, respectively [26].

From these observation results, the cavity patterns occurring in single-mode fibers can be classified into the four patterns shown in **Figure 2**, where  $l$  is the length of the cavity and  $\Lambda$  is the (periodic) cavity interval. The observed periodic cavity patterns belong to patterns (a)–(c) with the pattern depending on the value of  $l/\Lambda$ . The long non-periodic cavity pattern (filaments) can be considered as a sequence of two or more of pattern (d).

These cavities have been considered to be the result of either the classic Rayleigh instability caused by the capillary effect in the molten silica surrounding a vaporized fiber core [32] or the electrostatic repulsion between negatively charged layers induced at the plasma–molten silica interface [33, 34]. Although the capillary effect convincingly explains the formation mechanism of water droplets from a tap and/or bubbles through a water flow, this effect does not appear to apply to the cavity formation mechanism of a fiber fuse owing to the anomalously high viscosity of the silica glass [23, 33]. Yakovlenko proposed a novel cavity formation mechanism based on the formation of an electric charge layer on the interface between the liquid glass and plasma [33]. This charge layer, where the electrons adhere to the liquid glass surface, gives rise to a “negative” surface tension coefficient for the liquid layer. In the case of a negative surface tension coefficient, the deformation of the liquid surface proceeds, giving rise to a long bubble that is pressed into the liquid [33]. Furthermore, an increase in the charged surface due to the repulsion of similar charges results in the development of instability [33]. The instability emerges because the countercurrent flowing in the liquid causes the liquid to enter the region filled with plasma, and the extruded liquid forms a bridge. Inside the region separated from the front part of the fuse by this bridge, gas condensation and cooling of the molten silica glass occur [34]. A row of cavities is formed by the repetition of this process. Although Yakovlenko’s explanation of the formation of a long cavity and rows of cavities is very interesting, the concept of “negative” surface tension appears to be unfeasible in the field of surface science and/or plasma physics (see Appendix A).

Low-frequency plasma instabilities are triggered by moving the high-temperature front of a fiber fuse toward the light source. It is well known that such a low-frequency plasma instability behaves as a Van der Pol oscillator with instability frequency  $\omega_0$  [35–55]. Therefore, the oscillatory motion of the ionized gas

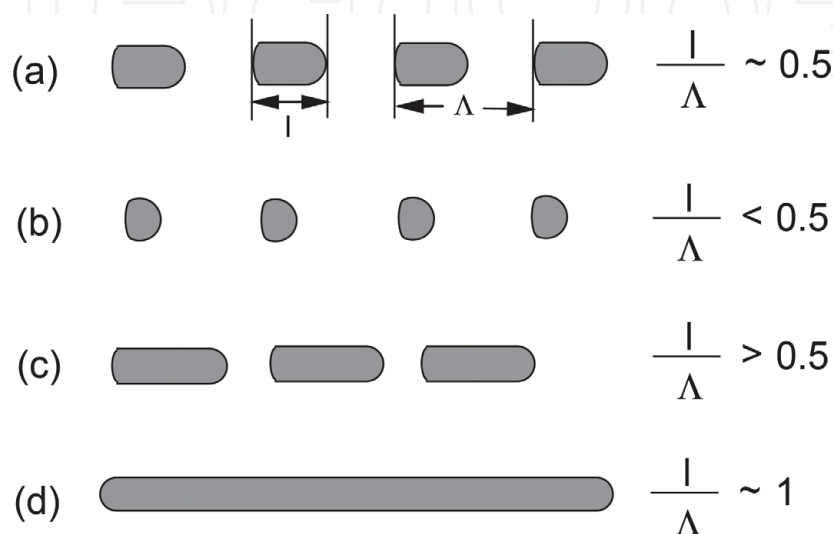


**Figure 2.**  
 Cavity patterns observed in optical fiber.

plasma during fiber fuse propagation can be studied phenomenologically using the Van der Pol equation [56].

In this paper the author describes a novel nonlinear oscillation model using the Van der Pol equation and qualitatively explains both the silica-glass densification and cavity formation observed in fiber fuse propagation. Furthermore, an investigation of the relationship between several cavity patterns and the nonlinearity parameters in the nonlinear oscillation model is reported.

## 2. Nonlinear oscillation behavior in ionized gas plasma

An ionized gas plasma exhibits oscillatory motion with a small amplitude when the high-temperature front of a fiber fuse propagates toward the light source.

The density  $\rho$  of the plasma is assumed to be in the form  $\rho = \rho_0 + \rho_1$ , where  $\rho_0$  is the initial density of the stationary (unperturbed) part in the front region of the plasma and  $\rho_1$  is the perturbed density. The dynamical behavior of  $\rho_1$  resulting from fiber fuse propagation can be represented by the Van der Pol equation

$$\frac{d^2\rho_1}{dt^2} - \varepsilon(1 - \beta\rho_1^2 + 2\gamma\rho_1)\frac{d\rho_1}{dt} + \omega_0^2\rho_1 = 0, \quad (1)$$

where  $\varepsilon$  is a parameter that characterizes the degree of nonlinearity and  $\beta$  characterizes the nonlinear saturation (see Appendix B). The nonlinearity parameter  $\gamma$  characterizes the oscillation pattern.

The angular frequency  $\omega_0$  of the oscillation of the gas plasma is determined by the ion-sound velocity  $C_s$  and the free-running distance  $L_f$  of the ion-sound wave, and is given by

$$\omega_0 = 2\pi f = 2\pi \frac{C_s}{L_f}. \quad (2)$$

where  $f$  is the frequency of the oscillation of the gas plasma. The ion-sound velocity  $C_s$  is given by [38]

$$C_s = \sqrt{\frac{RT_e}{M_i}}, \quad (3)$$

where  $R$  is the gas constant,  $T_e$  is the temperature of the electron, and  $M_i$  is the mass of the ion. The author estimated  $C_s = 1300$  m/s by using  $T_e = 5760$  K, which was the average temperature of the radiation zone [57], and  $M_i = 28 \times 10^{-3}$  kg for a  $\text{Si}^+$  ion. The free-running distance  $L_f$  was assumed to be 1.3 mm, which was almost equal to the distance (about 1.5 mm [57]) of the radiation zone. Using Eq. (2) and the  $C_s$  (= 1300 m/s) and  $L_f$  (= 1.3 mm) values, the frequency  $f$  of the oscillation was estimated to be about 1 MHz. The relatively high  $f$  or  $\omega_0$  values reported in the literature were 426–620 kHz [52, 53] and 14.5–40.9 MHz [35, 42, 45]. These relatively high frequencies are owing to the excitation of high-frequency electron oscillation together with ion oscillation in the ionized gas plasma. The  $f$  value (= 1 MHz) estimated above is comparable to these experimental values.

The oscillatory motion for  $\varepsilon = 0.1$ ,  $\beta = 6.5$ , and  $\gamma = 0$  was calculated using Eq. (1). The calculated result is shown in **Figure 3**, where the perturbed density  $\rho_1$  is plotted as a function of time. When  $t \geq 80\mu\text{s}$ , the maximum and minimum values of  $\rho_1$  for the ionized gas plasma reach 0.86 and  $-0.86$ , respectively. The maximum



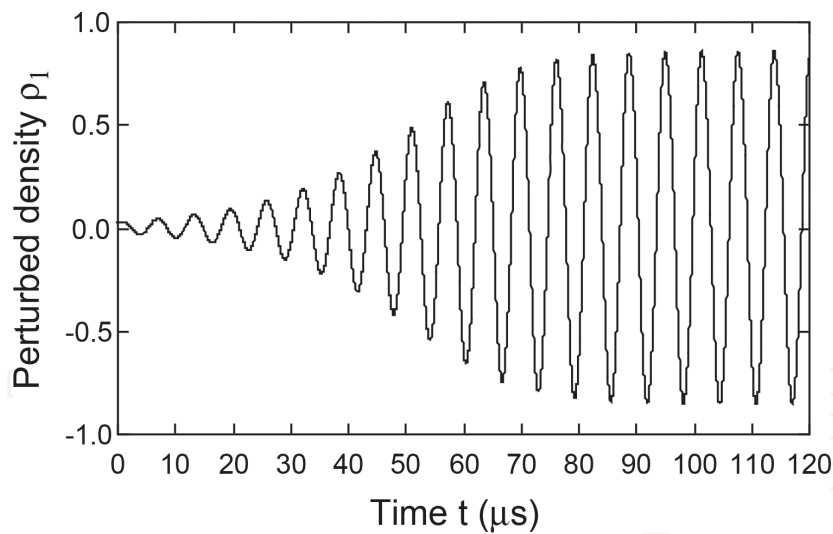


**Figure 3.**  
 Time dependence of the perturbed density during fiber fuse propagation.  $\varepsilon = 0.1$ ,  $\beta = 6.5$ ,  $\gamma = 0$ .

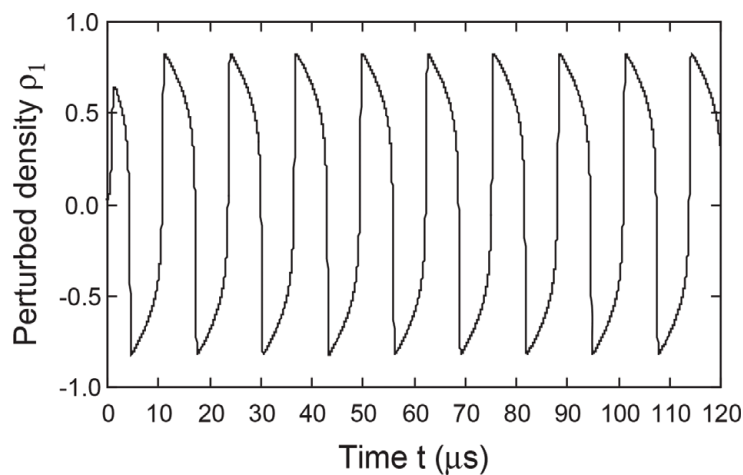


**Figure 4.**  
 Time dependence of the perturbed density during fiber fuse propagation.  $\varepsilon = 5$ ,  $\beta = 6.5$ ,  $\gamma = 0$ .

value (0.86) means that the increase in density of the core material reaches 86%, which is almost equal to the experimental value (87%) estimated by Dianov *et al.* [20].

On the other hand, it can be seen that for  $\varepsilon = 0.1$  the motion of the Van der Pol oscillator is very nearly harmonic, exhibiting alternate compression and rarefaction of the density with a relatively small period  $\Phi$  of about  $6.3 \mu\text{s}$ .

Next, the oscillatory motion for  $\varepsilon = 5, 9$ , and  $14$  with  $\beta = 6.5$  and  $\gamma = 0$  was examined. The calculated results are shown in **Figures 4–6**, respectively. It can be seen that for  $\varepsilon = 5, 9$ , and  $14$ , the oscillations consist of sudden transitions between compressed and rarefied regions. This type of motion is called a relaxation oscillation [56]. The  $\Phi$  values of the motion corresponding to  $\varepsilon = 5, 9$ , and  $14$  were estimated to be about  $12.9, 21.6$ , and  $36.1 \mu\text{s}$ , respectively. These  $\Phi$  values are much larger than that (about  $6.3 \mu\text{s}$ ) for  $\varepsilon = 0.1$ .

The oscillatory motion generated in the high-temperature front of the ionized gas plasma can be transmitted to the neighboring plasma at the rate of  $V_f$  when the fiber fuse propagates toward the light source. **Figure 7** shows a schematic view of the dimensional relationship between the temperature and the perturbed density of the ionized gas plasma during fiber fuse propagation.

In **Figure 7**,  $\Lambda$  is the interval between the periodic compressed (or rarefied) parts.

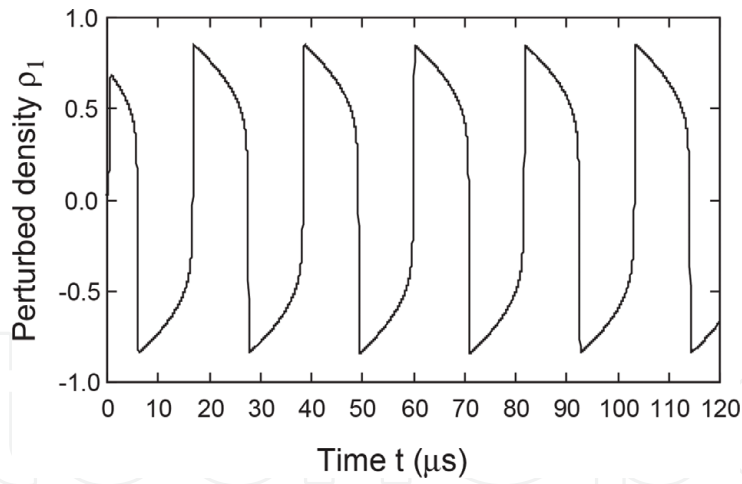


**Figure 5.**  
Time dependence of the perturbed density during fiber fuse propagation.  $\epsilon = 9$ ,  $\beta = 6.5$ ,  $\gamma = 0$ .

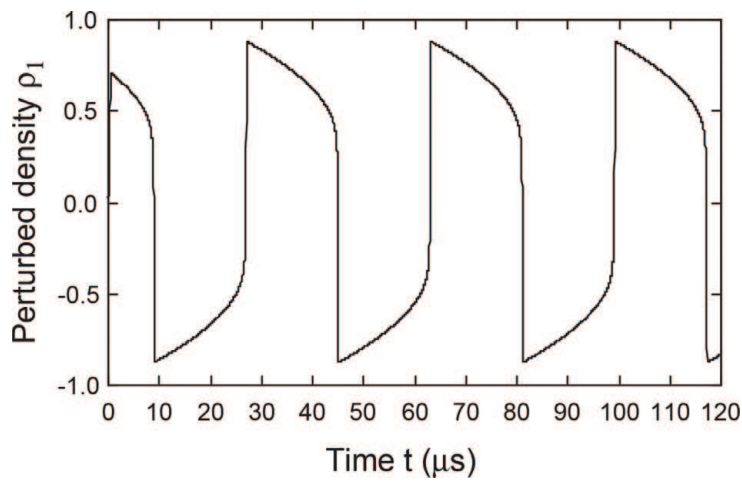


**Figure 6.**  
Time dependence of the perturbed density during fiber fuse propagation.  $\epsilon = 14$ ,  $\beta = 6.5$ ,  $\gamma = 0$ .

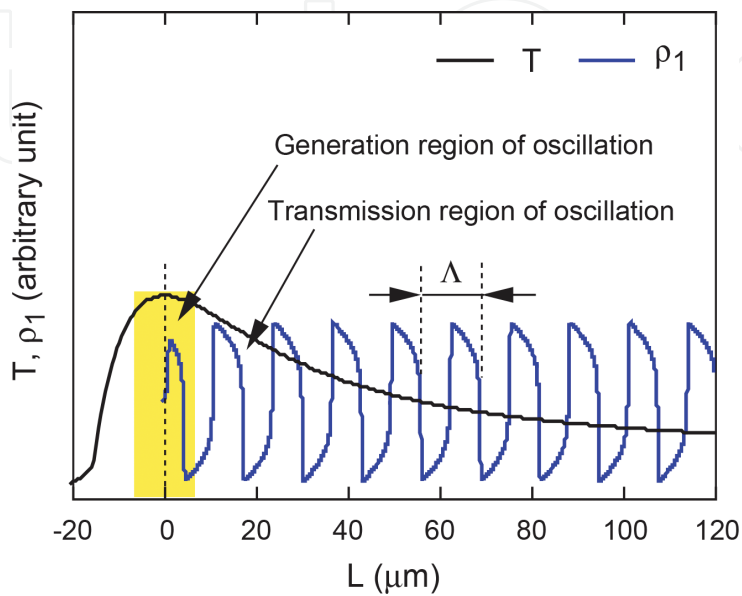


**Figure 7.**  
Schematic view of the dimensional relationship between the temperature and the perturbed density of the ionized gas plasma during fiber fuse propagation.

The relationship between the period  $\Phi$  and the interval  $\Lambda$  is

$$\Lambda = \Phi V_f, \quad (4)$$

where  $V_f$  is the propagation velocity of the fiber fuse and  $V_f = 1$  m/s was assumed in the calculation. The  $\Lambda$  values of the motion corresponding to  $\varepsilon = 5, 9,$  and  $14$  are thus estimated to be about  $12.9, 21.6,$  and  $36.1 \mu\text{m}$ , respectively, using Eq. (4) and  $V_f = 1$  m/s. If a large amount of molecular oxygen ( $\text{O}_2$ ) accumulates in the rarefied part, the periodic formation of bubbles (or cavities) will be observed. In such a case,  $\Lambda$  is equal to the periodic cavity interval. The estimated  $\Lambda$  values ( $12.9, 21.6,$  and  $36.1 \mu\text{m}$ ) are close to the experimental periodic cavity intervals of  $13\text{--}22 \mu\text{m}$  observed in fiber fuse propagation [13, 23].

**Figure 8** shows the relationship between  $\Phi$  and the nonlinearity parameter  $\varepsilon$ . As shown in **Figure 8**,  $\Phi$ , which is proportional to the interval  $\Lambda$ , increases with increasing  $\varepsilon$ . That is, the increase in  $\Phi$  and/or  $\Lambda$  occurs because of the enhanced nonlinearity. It was found that the experimental periodic cavity interval increases with the laser pump power [13, 23]. It can therefore be presumed that the nonlinearity of the Van der Pol oscillator occurring in the ionized gas plasma is enhanced with increasing pump power.

Kashyap reported that the cavity shape was dependent on the nature of the input laser light (CW or pulses) [7, 15]. Todoroki classified the damage to the front part of a fiber fuse into three shapes (two spheroids and a long partially cylindrical cavity) depending on the pump power [23]. He also found that a rapid increase or decrease in the pump power results in an increase in the length of the cavity-free segment or the occurrence of an irregular cavity pattern, respectively [26]. These findings indicate that the cavity shape and the regularity of the cavity pattern may be determined by the degree of nonlinearity of the Van der Pol oscillator.

In what follows, the results of examining the relationship between the interval  $\Lambda$  and the input laser power  $P_0$  observed in fiber fuse propagation are described.

## 2.1 Power dependence of periodic cavity interval

It is well known that the fiber-fuse propagation velocity  $V_f$  increases with increasing input laser power  $P_0$  [7, 8, 22, 23, 25, 26, 58–60]. Furthermore, in

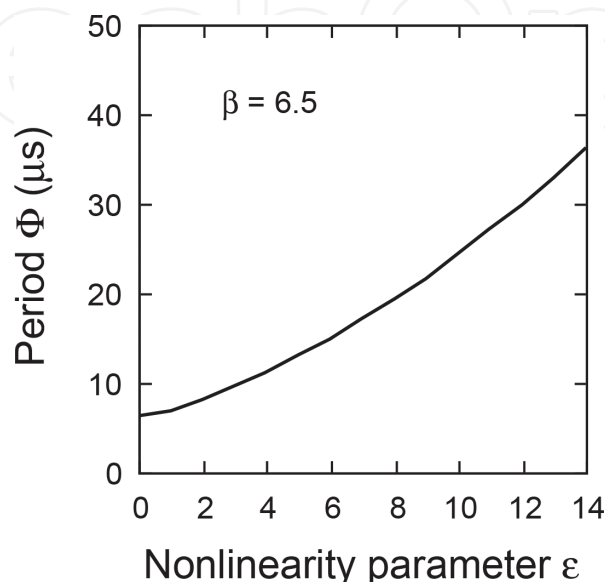


**Figure 8.**  
 Relationship between the period  $\Phi$  and the nonlinearity parameter  $\varepsilon$ .  $\beta = 6.5, \gamma = 0$ .



addition to  $V_f$ , Todoroki reported the  $P_0$  dependence of  $\Lambda$  in an SMF-28e fiber at  $\lambda_0 = 1.48 \mu\text{m}$  [13, 23].

In this study the author investigated the  $P_0$  dependence of  $\Lambda$  using the experimental  $V_f$  values [23, 26] and the calculated  $\Phi$  values shown in **Figure 8**.

To explain the experimental  $\Lambda$  values in the  $P_0$  range from the threshold power ( $P_{th} \approx 1.3\text{W}$  [61]) to 9 W,  $\Lambda(P_0)$  can be represented by

$$\Lambda(P_0) = \Phi_0 V_f(P_0) \left[ 1 - \zeta \frac{\sqrt{\Phi_n(\varepsilon) - \Phi_n(\varepsilon = 0)}}{\Phi_0} \right], \quad (5)$$

where  $\Phi_0$  and  $\zeta$  are constants and  $\Phi_n$  is the calculated  $\Phi$  value shown in **Figure 8**. The second term  $-\zeta \sqrt{\Phi_n(\varepsilon) - \Phi_n(\varepsilon = 0)} V_f(P_0)$  on the right of Eq. (5) represents the contribution of the nonlinearity to the overall  $\Lambda$  value.

On the other hand, the relationship between the nonlinearity parameter  $\varepsilon$  and  $P_0$  can be expressed as

$$\varepsilon = \chi(P_0 - P_{th})^{(m/2)}, \quad (6)$$

where  $\chi$  is a constant and  $m$  is the order of the square root of the power difference  $P_0 - P_{th}$ .  $\varepsilon$  and  $\chi$  correspond to the induced polarization and nonlinear susceptibility in nonlinear optics, respectively [62]. In the calculation, the author adopted  $\chi = 1$  and  $m = 2$ .

Using Eq. (5),  $\Phi_0 = 31.5 \mu\text{s}$ ,  $\zeta = 3.6$ , and the  $\Phi_n$  values shown in **Figure 8**, the  $\Lambda$  values were calculated as a function of  $P_0$ . The calculated results are shown in **Figure 9**. The blue solid line in **Figure 9** is the curve calculated using

$$\Lambda(P_0) = \Phi_0 V_f(P_0), \quad (7)$$

which is the first term on the right of Eq. (5).

As shown in **Figure 9**,  $\Lambda$  increases abruptly near the threshold power ( $P_{th}$ ) and increases with increasing  $P_0$ . The  $\Lambda$  values at  $P_0 = 2.0\text{--}2.5\text{ W}$  satisfy Eq. (7).

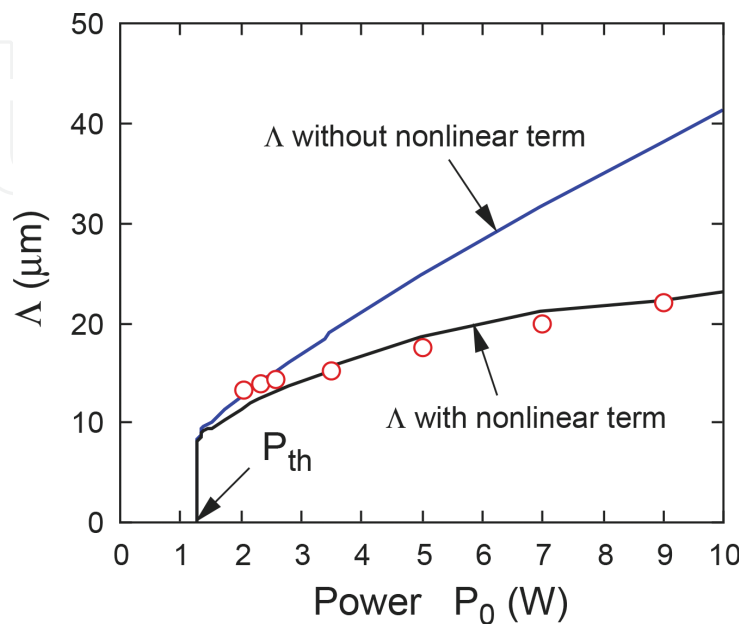


**Figure 9.** Relationship between the interval  $\Lambda$  and the input power  $P_0$ . The blue and black solid lines were calculated using Eqs. (7) and (5), respectively. The red open circles are the data reported by Todoroki [23, 26].

However, with increasing  $P_0$ , the  $\Lambda$  values at  $P_0 > 2.5$  W are less than those calculated using Eq. (7) and approach the  $\Lambda$  values estimated using Eq. (5).

This may be related to the modes of fiber fuse propagation reported by Todoroki [23, 26]. Todoroki classified the damage to the front part of a fiber fuse into three shapes (two spheroids and a long partially cylindrical cavity) depending on the pump power, and the appearance of the long partially cylindrical cavity was observed at  $P_0 > 3.5$  W [23] or  $P_0 > 2.3$  W [26]. As shown in **Figure 9**, the distinct contribution of the nonlinearity to the overall  $\Lambda$  value begins at  $P_0$  of 2.3–3.5 W, and the oscillatory motion of the gas plasma changes from a nearly harmonic oscillation (see **Figure 3**) to a relaxation oscillation (see **Figure 4**) with increasing  $P_0$ . Therefore, the change from the spheroids of unstable and unimodal modes to the long partially cylindrical cavities of the cylindrical mode may be related to the contribution of the nonlinearity.

### 3. Effect of nonlinearity parameters on cavity patterns

The nonlinearity parameter  $\gamma$  characterizes the oscillation pattern. The oscillatory motion for  $\varepsilon = 9$ ,  $\beta = 6.5$ , and  $\gamma = 0$  was shown in **Figure 5**, where the perturbed density  $\rho_1$  is plotted as a function of time. It can be seen in **Figure 5** that the oscillations consist of sudden transitions between compressed and rarefied regions, and the retention time  $\tau_r$  of the rarefied regions equals that of the compressed regions  $\tau_c$ . The relationship between the period  $\Phi$  ( $= \tau_r + \tau_c$ ) and the interval  $\Lambda$  is given by Eq. (4), and the relationship between  $\tau_r$  and the length  $l$  of the cavity is

$$l = \tau_r V_f. \quad (8)$$

The  $\Lambda$  and  $l$  values of the motion corresponding to  $\varepsilon = 9$ ,  $\beta = 6.5$ , and  $\gamma = 0$  are estimated to be about 10.8 and 21.6  $\mu\text{m}$ , respectively, using Eqs. (4) and (8) and  $V_f = 1$  m/s. That is,  $l/\Lambda = 0.5$  in the case of  $\gamma = 0$ .

Next, the oscillatory motion for  $\gamma = 2$  and  $-2$  with  $\varepsilon = 9$  and  $\beta = 6.5$  was examined. The calculated results are shown in **Figures 10** and **11**, respectively. As shown in **Figure 10**, the retention time  $\tau_r$  of the rarefied regions is larger than that of the compressed regions  $\tau_c$ . As a result, the ratio  $l/\Lambda$  is larger than 0.5 in the case of

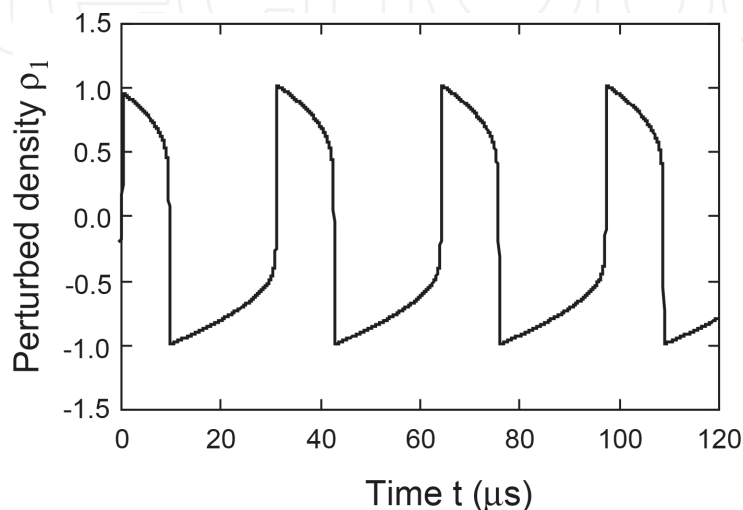


**Figure 10.** Time dependence of the perturbed density during fiber fuse propagation.  $\varepsilon = 9$ ,  $\beta = 6.5$ ,  $\gamma = 2$ .

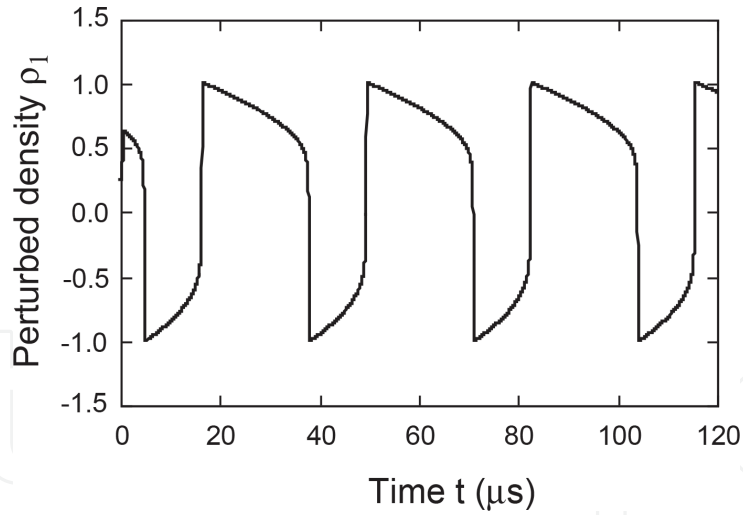


**Figure 11.** Time dependence of the perturbed density during fiber fuse propagation.  $\varepsilon = 9$ ,  $\beta = 6.5$ ,  $\gamma = -2$ .

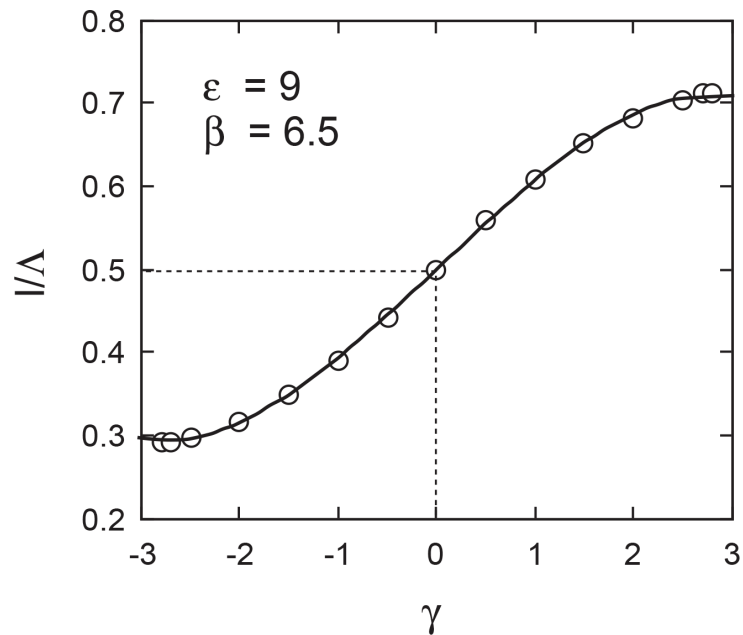


**Figure 12.** Relationship between  $l/\Lambda$  and the nonlinearity parameter  $\gamma$ .  $\varepsilon = 9$ ,  $\beta = 6.5$ .

$\gamma = 2$ . On the other hand, as shown in **Figure 11**,  $\tau_r$  is smaller than  $\tau_c$  and  $l/\Lambda < 0.5$  in the case of  $\gamma = -2$ .

**Figure 12** shows the relationship between  $l/\Lambda$  and the nonlinearity parameter  $\gamma$ . As shown in **Figure 12**,  $l/\Lambda$  increases with increasing  $\gamma$  and approaches its maximum value (about 0.71) at  $\gamma \sim 2.8$ . In contrast,  $l/\Lambda$  approaches its minimum value (about 0.29) at  $\gamma \sim -2.8$ .

### 3.1 Deformation of cladding due to plasma formation

The inside of the high-temperature core of 4,000–10,000 K has a high internal pressure  $p$  of  $1 \times 10^4$ – $5 \times 10^4$  atm [18]. The inner wall of the core (in the solid state) will be expanded by this internal pressure  $p$ . To simplify the calculation, the existence of molten silica glass (liquid state) between the solid-state cladding layer (inner radius  $r_i$ , outer radius  $r_f$ ) and the inner high-pressure gas plasma is ignored [33].

$r_i$  for the cladding is assumed to be  $d_{melted}/2$ . With increasing inner pressure  $p$ , the inner radius of the cladding layer increases in the radial direction owing to the

compression of the cladding layer. The increment  $\delta r$  in the radius  $r$  of the solid-state cladding layer can be expressed in terms of the Young's modulus  $E$  and Poisson's ratio  $\nu$  of the (solid-state) silica glass, and is given by the following equation [63].

$$\delta r = \frac{r_i^2 p}{E(r_f^2 - r_i^2)} \left[ (1 - \nu) + (1 + \nu) \frac{r_f^2}{r^2} \right] \cdot r \quad (9)$$

Todoroki reported that  $d_{melted}$  and the diameter  $d$  of periodic cavities with  $\Lambda \sim 22 \mu m$ , which is equal to that in the case of  $\varepsilon = 9$  and  $\gamma = 0$ , were about 20 and  $6.5 \mu m$ , respectively [13]. We adopted  $r_i = d_{melted}/2 \cong 10 \mu m$  and  $r_f = 62.5 \mu m$ . Using  $E = 73$  GPa and Poisson's ratio  $\nu = 0.17$  for silica glass, the relationship between  $\delta r/r_i$  and  $r/r_i$  at  $p = 2$  GPa ( $=1.97 \times 10^4$  atm) is calculated. The results are shown in **Figure 13**. It can be clearly seen from **Figure 13** that the elongation rate  $\delta r/r_i$  of the inner radius has a maximum value (about 3.35%) when  $r/r_i$ .

We consider the tensile stress  $\sigma_\theta$  acting on the inner wall ( $r = r_i$ ) of the cladding layer.  $\sigma_\theta$  is related to  $p$  by the following expression [63]:

$$\sigma_\theta = \frac{r_f^2 + r_i^2}{r_f^2 - r_i^2} \cdot p. \quad (10)$$

$\sigma_\theta$  increases with increasing  $p$ . Using  $r_i \sim 10 \mu m$  and  $r_f = 62.5 \mu m$ ,  $\sigma_\theta$  was estimated to be about 2.1 GPa when  $p = 2$  GPa. If this  $\sigma_\theta$  value exceeds the ideal fracture strength  $\sigma_0$  of the silica glass, a crack will be generated on the inner wall of the cladding layer.

On the other hand, it is well known for various solid materials that the  $\sigma_0$  value is related to the Young's modulus  $E$  of the material by the following equation [64]:

$$\sigma_0 \approx E/10. \quad (11)$$

By using Eq. (11) and  $E = 73$  GPa for silica glass, we can estimate  $\sigma_0$  to be approximately 7.3 GPa. Since this value is larger than the estimated  $\sigma_\theta$  value (2.1 GPa), the cladding layer is never broken, but it can be seen that a relatively large expansion of the inner radius occurs as a result of the internal pressure.

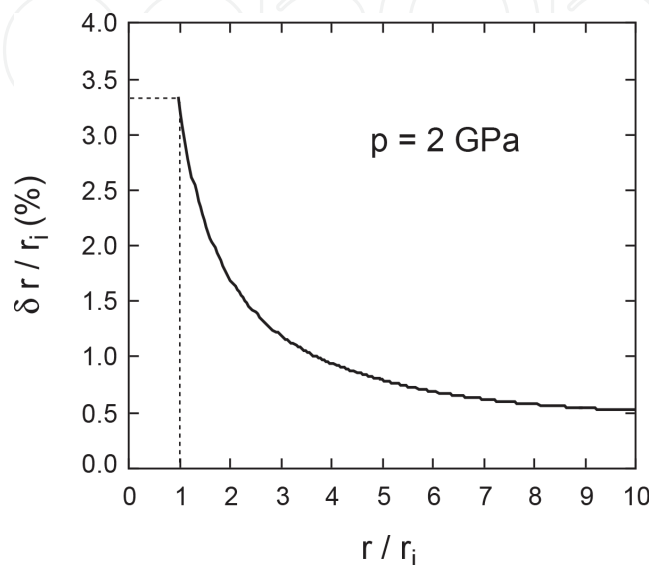


**Figure 13.**  
 Relationship between  $\delta r/r_i$  and  $r/r_i$ .

The excess volume  $\Delta V$  produced by the expansion of the inner radius over the interval  $\Lambda$  of the cavity can be estimated as follows using the maximum  $\delta r$  value  $\delta r_{max}$  at  $r = r_i$ :

$$\Delta V = \Lambda \pi \left[ (r_i + \delta r_{max})^2 - r_i^2 \right]. \quad (12)$$

As the maximum elongation rate  $\delta r_{max}/r_i$  was about 3.35% (see **Figure 13**),  $\delta r_{max}$  was estimated to be about  $0.335 \mu m$  by using  $r_i \cong 10 \mu m$ .

On the other hand, the volume  $V$  of a cavity with diameter  $d$  and length  $l$  is given by

$$V = l \pi \left( \frac{d}{2} \right)^2. \quad (13)$$

It is considered that the volume required to generate a cavity was compensated by the excess volume  $\Delta V$  [33]. If the value of  $V$  required to generate a cavity in the interval  $\Lambda$  is smaller than  $\Delta V$ , the oscillation pattern predicted by Eq. (1) will be maintained and periodic cavities having a size corresponding to  $V$  will be formed in the core. That is, the necessary condition for the formation of a periodic cavity pattern is that the ratio of  $V$  to  $\Delta V$  is smaller than 1, which is expressed as follows:

$$\frac{V}{\Delta V} = \frac{l}{\Lambda} \frac{d^2}{4 \delta r_{max} (2r_i + \delta r_{max})} \leq 1. \quad (14)$$

Rearranging Eq. (14), we obtain the following inequality for  $l/\Lambda$ :

$$\frac{l}{\Lambda} \leq \frac{4}{d^2} \delta r_{max} (2r_i + \delta r_{max}). \quad (15)$$

When  $r_i \sim 10 \mu m$ ,  $\delta r_{max} \sim 0.335 \mu m$ , and  $d \sim 6.5 \mu m$ , we obtain

$$\frac{l}{\Lambda} \leq 0.645.$$

When  $l/\Lambda$  satisfies this condition, the periodic cavities predicted by Eq. (1) will be formed in the core.

However, as shown in **Figure 12**,  $l/\Lambda$  can be larger than 0.645 when  $\gamma > 1.5$ . In this case, the cavities formed in the core will be compressed and deformed as shown in **Figure 14**.

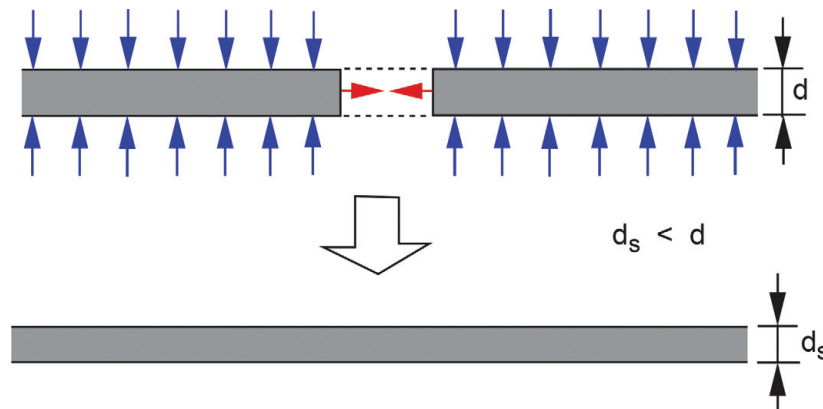


**Figure 14.** Schematic view of cavity compression and deformation in core.



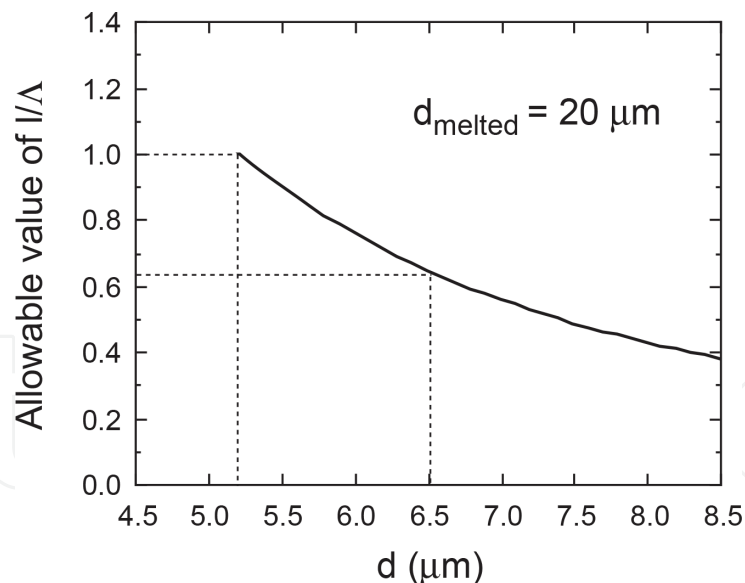


**Figure 15.** Relationship between the maximum allowable value of  $l/\Lambda$  and the cavity diameter  $d$ .  $d_{\text{melted}} = 20 \mu\text{m}$ .

As shown in Eq. (15), the allowable value of  $l/\Lambda$  increases with decreasing cavity diameter  $d$ . **Figure 15** shows the relationship between the maximum allowable value of  $l/\Lambda$  and the diameter  $d$ . As shown in **Figure 15**, when  $d$  is reduced by 20% from 6.5 to 5.2  $\mu\text{m}$ , we obtain.

$$\frac{l}{\Lambda} \leq 1.$$

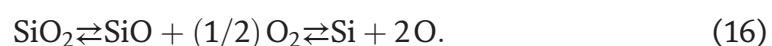
Under this condition, cavity pattern (d) (long filaments) in addition to periodic pattern (c) in **Figure 2** can be formed in the core. As the number of repetitions of pattern (d) can change freely, the period of long filaments can be irregular. This may be the cause of the long non-periodic filaments observed by several researchers [20–22, 32].

Kashyap reported that the diameter of a short asymmetric cavity with  $l/\Lambda < 0.5$  was larger than that of an oblong and cylindrically symmetric cavity with  $l/\Lambda$  of about 0.5 and that the diameter of a long bullet-shaped cavity with  $l/\Lambda < 0.5$  was smaller than that of the cavities described above [7]. These findings are consistent with the calculation results shown in **Figure 15**. In what follows, the production and diffusion of  $\text{O}_2$  gas in the high-temperature core layer are described.

### 3.2 Oxygen production in optical Fiber

When gaseous  $\text{SiO}$  and/or  $\text{SiO}_2$  molecules are heated to high temperatures of above 5,000 K, they decompose to form Si and O atoms, and finally become  $\text{Si}^+$  and  $\text{O}^+$  ions and electrons in the ionized gas plasma state.

In a confined core zone, and thus at high pressures,  $\text{SiO}_2$  is decomposed with the evolution of  $\text{SiO}$  gas or Si and O atomic gases at elevated temperatures [65]:



The number densities  $N_{\text{SiO}}$ ,  $N_{\text{Si}}$ , and  $N_{\text{O}}$  (in  $\text{cm}^{-3}$ ) can be estimated using the procedure described in [57, 66] and the published thermochemical data [67] for Si,  $\text{SiO}$ , O,  $\text{O}_2$ , and  $\text{SiO}_2$ .

The dependence of  $N_{\text{O}}$  on the temperature  $T$  is shown in **Figure 16**.  $N_{\text{O}}$  gradually approaches its maximum value ( $3.3 \times 10^{21} \text{cm}^{-3}$ ) at 11,100 K and then decreases

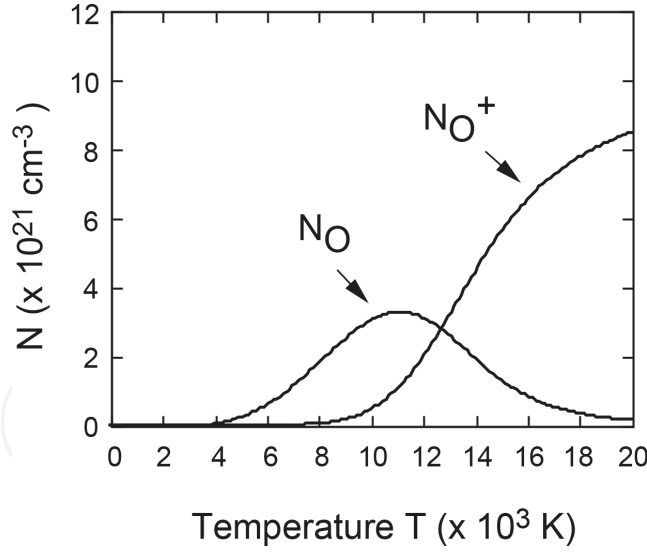


**Figure 16.**  
Temperature dependences of the number densities of O and O<sup>+</sup>.

with further increasing  $T$ . This is because oxygen (O) atoms are ionized to produce O<sup>+</sup> ions and electrons in the ionized gas plasma as follows:



The number density  $N_{\text{O}^+}$  of O<sup>+</sup> ions can be estimated using the Saha equation [66, 68]:

$$\frac{N_{\text{O}^+}^2}{N_{\text{O}}} \approx 2 \frac{(2\pi m_e kT)^{3/2}}{h^3} \frac{Z_+}{Z_0} \exp(-I_p/k_B T), \quad (18)$$

where  $I_p$  (= 13.61 eV [69]) is the ionization energy of a neutral O atom,  $m_e$  is the electron mass,  $h$  is Planck's constant, and  $k_B$  is Boltzmann's constant.  $Z_+$  and  $Z_0$  are the partition functions of ionized atoms and neutral atoms, respectively, and  $Z_+ \approx Z_0$ . The relationship between  $N_{\text{O}^+}$  and  $T$  is also shown in **Figure 16**.  $N_{\text{O}^+}$  increases gradually at temperatures above 7,000 K and reaches  $8.9 \times 10^{21} \text{ cm}^{-3}$  at  $2 \times 10^4 \text{ K}$ .

It has been found that molecular oxygen is released and remains in the cavities of a damaged core layer while maintaining a relatively high pressure (about 4 atm [7] or 5–10 atm [20]) at room temperature. The molecular oxygen (O<sub>2</sub>) is produced from neutral O atoms as follows:



The rate equation of this reaction is [70]

$$\frac{dN_{\text{O}_2}}{dt} = \sqrt{2\pi}\sigma^2 \sqrt{\frac{8RT}{\pi M_{\text{O}}}} N_{\text{O}}^2 \exp(-E_a/RT), \quad (20)$$

where  $\sigma$  (= 1.5 Å) is half of the collision diameter,  $M_{\text{O}}$  (=  $16.0 \times 10^{-3} \text{ kg}$ ) is the atomic weight of O, and  $E_a$  is the activation energy. The bond energy (493.6 kJ/mol [71]) of oxygen was used for  $E_a$ .

The dependence of  $dN_{\text{O}_2}/dt$  on the temperature  $T$  is shown in **Figure 17**. The rate of O<sub>2</sub> production  $dN_{\text{O}_2}/dt$  exhibits its maximum value ( $2.96 \times 10^{31} \text{ cm}^{-3}\text{s}^{-1}$ ) at 12,700 K. This means that the oxygen molecules are produced most effectively at 12,700 K.

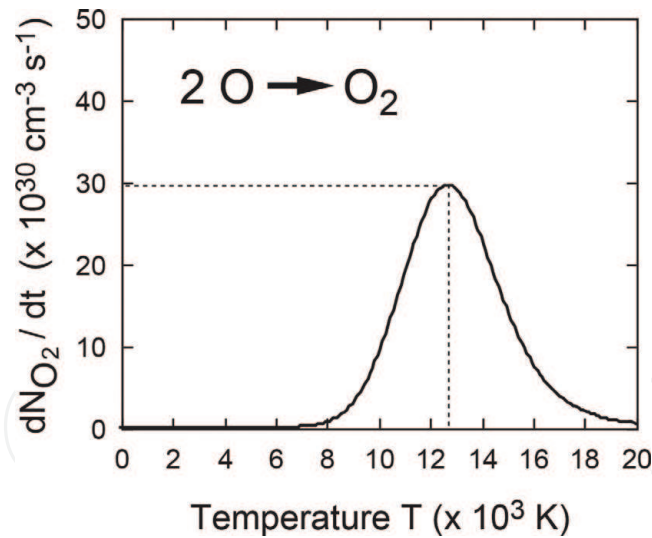


**Figure 17.**  
 Temperature dependence of the production rate of O<sub>2</sub>.

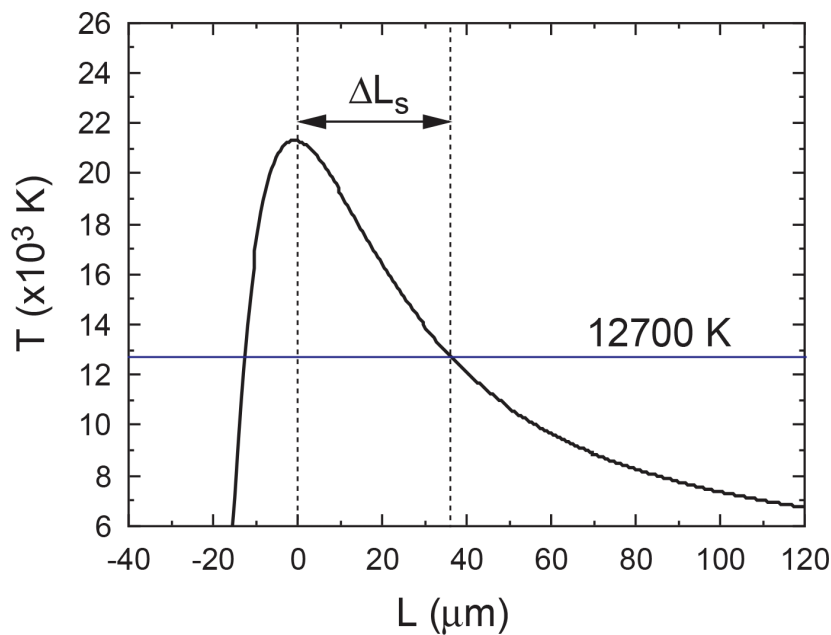


**Figure 18.**  
 Temperature distribution of the high-temperature front versus the length along the  $z$  direction at  $t = 3$  ms after the incidence of 1.8 W laser light for  $IA = 8$  dB. The center of the high-temperature front is set at  $L = 0$   $\mu\text{m}$ .

**Figure 18** shows the temperature distribution of the high-temperature front along the  $z$  direction at  $t = 3$  ms after the incidence of 1.8 W laser light for  $IA = 8$  dB. The calculation of the temperature distribution was described in Ref. [72]. In **Figure 18** the initial attenuation  $IA$  of 8 dB corresponds to an optical absorption coefficient  $\alpha$  of  $1.84 \times 10^6 \text{ m}^{-1}$  when the thickness of the absorption layer, which consists of carbon black, is about  $1 \mu\text{m}$  [72]. In this figure, the center of the high-temperature front is set at  $L = 0 \mu\text{m}$ . As shown in **Figure 18**,  $\Delta L_s$ , which is about  $36.5 \mu\text{m}$ , is the distance between the high-temperature peak ( $L = 0 \mu\text{m}$ ) and the location with a temperature of 12,700 K.

This  $\Delta L_s$  can be converted into the time lag  $\Delta\tau_s$  from the passage of the high-temperature front as follows:

$$\Delta\tau_s = \frac{\Delta L_s}{V_f}. \quad (21)$$

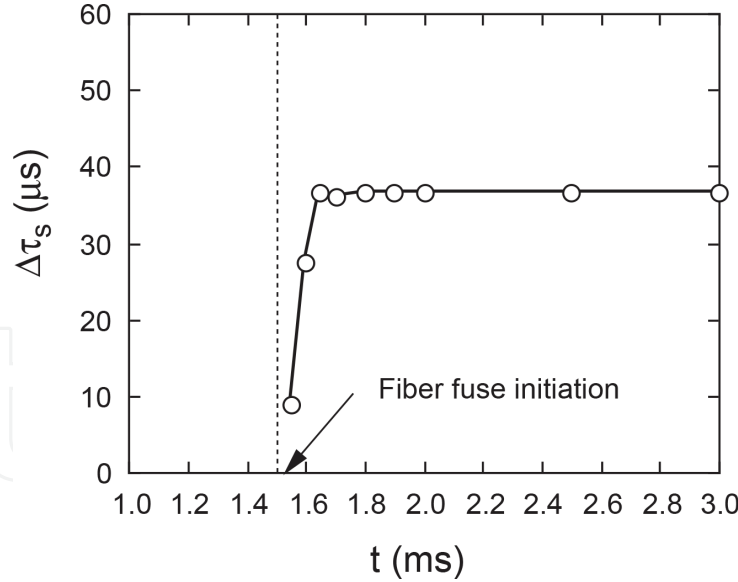


**Figure 19.**  $\Delta\tau_s$  values versus  $t$  after the incidence of 1.8 W laser light for  $IA = 8$  dB.

It is expected that the  $O_2$  molecular gas in the ionized gas plasma will be observed most frequently after a time lag of  $\Delta\tau_s$  from the passage of the high-temperature peak. If the produced  $O_2$  gas diffuses into the rarefied part of the oscillatory variation in density shown in **Figures 4–6, 10, and 11**, periodic cavities containing some of the oxygen molecules will be formed (see below).

When  $V_f = 1$  m/s, the  $\Delta\tau_s$  values were estimated at a time of  $t = 1.55$ – $3$  ms after the incidence of 1.8 W laser light for  $IA = 8$  dB. The calculated  $\Delta\tau_s$  values are plotted in **Figure 19** as a function of  $t$ . The fiber fuse phenomenon was initiated at  $t = 1.5$  ms (see **Figure 14** in Ref. [72]). As shown in **Figure 19**,  $\Delta\tau_s$  increases rapidly with increasing  $t$  immediately after the fiber fuse is initiated and reaches a constant value ( $36.5 \mu\text{s}$ ) at  $t > 1.65$  ms. This value is in reasonable agreement with the experimental values ( $20$ – $70 \mu\text{s}$ ) reported by Dianov and coworkers [30, 31].

### 3.3 Diffusion length of oxygen gas

The  $O_2$  gas produced near the high-temperature front diffuses from the compressed part into the rarefied part of the oscillatory variation during a short period  $\Phi$  of  $10$ – $30 \mu\text{s}$  (see **Figure 8**).

The diffusion coefficient  $D$  of the  $O_2$  gas is given by [70].

$$D = \frac{2}{3\pi\sigma^2 N_{O_2}} \sqrt{\frac{RT}{\pi M_{O_2}}}, \quad (22)$$

where  $M_{O_2} (= 32.0 \times 10^{-3} \text{ kg})$  is the molecular weight of  $O_2$  gas. As  $N_{O_2}$  is smaller than  $N_O/2$ ,  $N_{O_2} \approx N_O/2$  is assumed in the calculation.

The mean square of the displacement  $\Delta\bar{z}^2$  along the  $z$  direction of the optical fiber can be estimated from  $D$  and time  $t$  as follows [73]:

$$\Delta\bar{z}^2 = 2Dt. \quad (23)$$

The  $\Delta\bar{z}$  values at  $T = 12,700$  K were estimated using Eqs. (16) and (17). When  $t = 20 \mu\text{s}$ , the calculated  $\Delta\bar{z}$  value is given by

$$\Delta\bar{z} = \pm 16.7 \mu\text{m}.$$

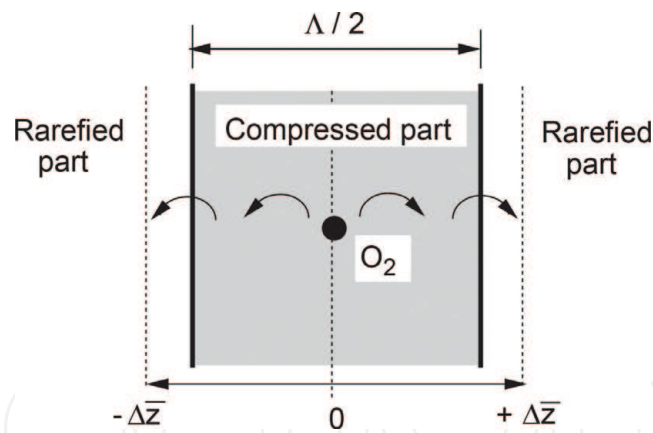


**Figure 20.** Schematic view of diffusion of oxygen gas from the compressed part into the rarefied part in the high-temperature plasma.

This  $\Delta\bar{z}$  value is of the same order as the observed periodic cavity interval (13–22  $\mu\text{m}$ ) [13].

**Figure 20** shows a schematic view of the diffusion of the  $\text{O}_2$  gas from the compressed part into the rarefied part in the high-temperature plasma. If the absolute value of  $\Delta\bar{z}$  is larger than half of the interval  $\Lambda$  between the periodic rarefied parts, many of the  $\text{O}_2$  molecules produced in the compressed part can move into the rarefied part during the period  $\Phi$  (10–30  $\mu\text{s}$ ) of the relaxation oscillation. This  $\text{O}_2$  gas will form temporary microscopic cavities that can constitute the nuclei necessary for growth into macroscopic bubbles [74].

As described above, the nonlinear oscillation model was able to phenomenologically explain both the densification of the core material and the formation of periodic cavities in the core layer as a result of the relaxation oscillation and the formation of  $\text{O}_2$  gas near the high-temperature front.

## 4. Conclusion

The evolution of a fiber fuse in a single-mode optical fiber was studied theoretically. To clarify both the silica-glass densification and cavity formation, which are observed in fiber fuse propagation, we investigated a nonlinear oscillation model using the Van der Pol equation. This model was able to phenomenologically explain the densification of the core material, the formation of periodic cavities, the cavity shape, and the regularity of the cavity pattern in the core layer as a result of the relaxation oscillation and cavity compression and/or deformation.

This nonlinear oscillation model including the relaxation oscillation is a phenomenological model, and the relationship between the nonlinearity parameters ( $\epsilon$ ,  $\beta$ ,  $\gamma$ ) and the physical properties observed in the fiber fuse experiments is unknown. Therefore, to clarify this relationship, further quantitative investigation is necessary.

### A. Electrostatic interaction between charged surface and plasma

In a confined core zone, and thus at a high pressure,  $\text{SiO}_2$  is decomposed with the evolution of  $\text{SiO}$  gas or  $\text{Si}$  and  $\text{O}$  atomic gases at elevated temperatures, as described in the main text. When the  $\text{Si}$  and  $\text{O}$  atomic gases are heated to high



temperatures of above 3,000 K (Si) and 4,000 K (O), they are ionized to produce  $\text{Si}^+$  and  $\text{O}^+$  ions and electrons in the ionized gas plasma state.



If thermally produced electrons in the plasma are not bound to positive species ( $\text{Si}^+$  or  $\text{O}^+$  ions), they can move freely in the plasma under the action of the alternating electric field of the light wave. Such free diffusion is possible only in the limiting case of very low charge densities. However, as shown in **Figure 16** and also **Figure 1** in Ref. [66], the densities of  $\text{Si}^+$  and  $\text{O}^+$  ions and electrons are reasonably large above  $1 \times 10^4$  K. At high charge densities, it is known that the positive and negative species diffuse at the same rate. This phenomenon, proposed by Schottky [75], is called ambipolar diffusion [76, 77]. Ambipolar diffusion is the diffusion of positive and negative species owing to their interaction via an electric field (space-charge field). In plasma physics, ambipolar diffusion is closely related to the concept of quasineutrality.

Some electrons arrive at the surface of melted silica glass, and they attach to oxygen atoms on the surface because oxygen atoms have a high electron affinity [78]. As a result, a negatively charged surface, which was proposed by Yakovlenko [33], may be formed as shown in **Figure 21**.

However, the negative charges on the surface will immediately be balanced by an equal number of oppositely charged  $\text{Si}^+$  and  $\text{O}^+$  ions because these positive ions move together with the electrons as a result of ambipolar diffusion. In this way, an atmosphere of ions is formed in the rapid thermal motion close to the surface. This ionic atmosphere is known as the diffuse electric double layer [79].

The thickness  $\delta_0$  of the double layer is approximately  $1/\kappa$ , which is the characteristic length known as the Debye length. The parameter  $\kappa$  is given in terms of  $N_e$  and  $T$  as follows [77]:

$$\kappa^2 = \frac{2N_e e^2}{\epsilon_0 k_B T}, \quad (25)$$

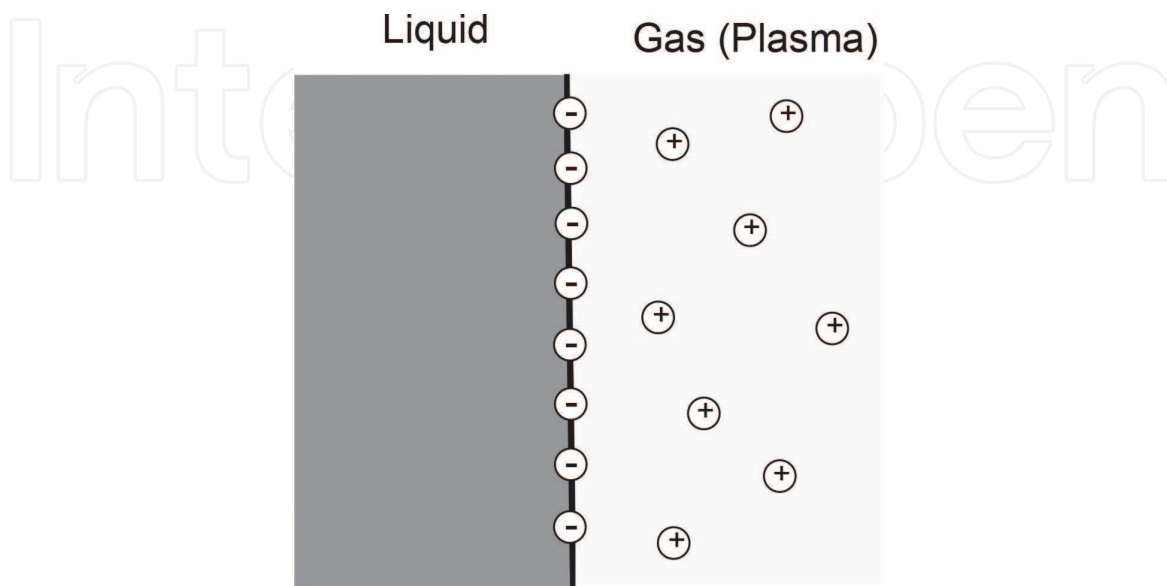


**Figure 21.** Schematic view of the negatively charged surface and ionic atmosphere.

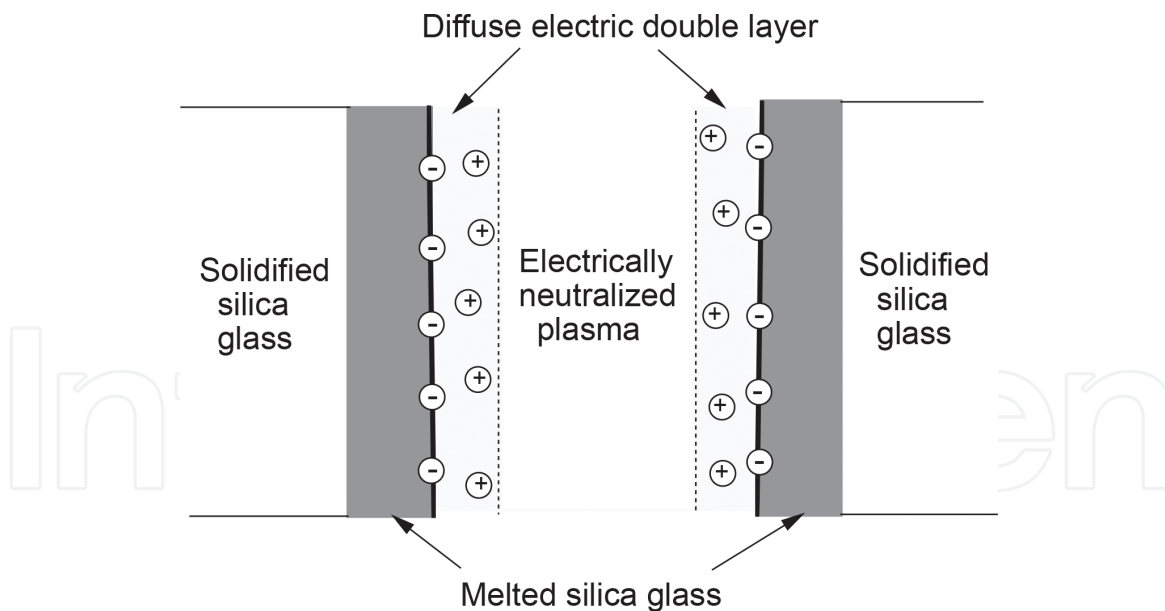


**Figure 22.**  
 Schematic view of the cross section of the high-temperature plasma in the optical fiber.

where  $e$  is the charge of an electron and  $\varepsilon_0$  is the dielectric constant of vacuum. When  $T = 1 \times 10^4$  K,  $N_e = 2.2 \times 10^{20}$  cm<sup>-3</sup>. Using these values and Eq. (25), the thickness  $\delta_0$  of the double layer at  $1 \times 10^4$  K was estimated to be about  $3.3 \times 10^{-10}$  m.

A cross section of the high-temperature plasma in the optical fiber with the double layers is schematically shown in **Figure 22**.

In the central domain of the high-temperature plasma, electrically neutral atoms (Si and O) and charged species (Si<sup>+</sup>, O<sup>+</sup>, and e<sup>-</sup>) exist. As the charged species are balanced, electrical neutrality is achieved in the domain. Moreover, the dimensions of the domain are almost equal to those of the high-temperature plasma excluding the very thin (Å order) electric double layers at the surface of the melted silica glass.

## B. Nonlinearity parameter $\beta$ in Van der pol equation

The dynamical behavior of the perturbed density  $\rho_1$  resulting from fiber fuse propagation can be represented by the Van der Pol equation

$$\ddot{\rho}_1 - \varepsilon(1 - \beta\rho_1^2)\dot{\rho}_1 + \omega_0^2\rho_1 = 0, \quad (26)$$

where  $\ddot{\rho}_1 = d^2\rho_1/dt^2$ ,  $\dot{\rho}_1 = d\rho_1/dt$ ,  $\varepsilon$  and  $\beta$  are nonlinearity parameters, and the nonlinearity parameter  $\gamma = 0$  is assumed.

If the solution of Eq. (26) is written as

$$\rho_1 = A \cos(\omega_0 t + \varphi), \quad (27)$$

where the amplitude  $A$  and phase  $\varphi$  are slowly varying functions, then  $A$  satisfies the following equation:

$$A^2 = \rho_1^2 + \left(\frac{\dot{\rho}_1}{\omega_0}\right)^2. \quad (28)$$

Differentiating Eq. (28), we obtain

$$\begin{aligned}
 \dot{A} &= \frac{\dot{\rho}_1}{\omega_0^2 A} (\ddot{\rho}_1 + \omega_0^2 \rho_1) \\
 &= \frac{\dot{\rho}_1}{\omega_0^2 A} [\varepsilon(1 - \beta \rho_1^2) \dot{\rho}_1] \\
 &= \frac{\varepsilon}{\omega_0^2 A} (\dot{\rho}_1^2) - \frac{\varepsilon \beta}{\omega_0^2 A} \rho_1^2 (\dot{\rho}_1^2) \\
 &= \varepsilon A \sin^2(\omega_0 t + \varphi) - \varepsilon \beta A^3 \sin^2(\omega_0 t + \varphi) \cos^2(\omega_0 t + \varphi) \\
 &= \frac{\varepsilon}{2} A [1 - \cos(2\omega_0 t + 2\varphi)] - \frac{\varepsilon \beta}{8} A^3 [1 - \cos(4\omega_0 t + 4\varphi)].
 \end{aligned} \tag{29}$$

Because of the slowly varying property of  $A$ , the oscillatory terms  $A \cos(2\omega_0 t + 2\varphi)$  and  $A^3 \cos(4\omega_0 t + 4\varphi)$  on the right of Eq. (29) are averaged out every cycle and can be discarded [80], thus reducing Eq. (29) to

$$\begin{aligned}
 \dot{A} &\simeq \frac{\varepsilon}{2} A - \frac{\varepsilon \beta}{8} A^3 \\
 &\simeq \frac{\varepsilon}{2} A \left(1 - \frac{\beta}{4} A^2\right).
 \end{aligned} \tag{30}$$

The maximum value of  $A$ ,  $A_m$ , is obtained under the condition of  $\dot{A} = 0$ . To satisfy this condition,

$$A_m = \frac{2}{\sqrt{\beta}}. \tag{31}$$


This means that the nonlinearity parameter  $\beta$  determines the maximum and minimum values of  $\rho_1$ . In the calculation, we used  $\beta = 6.5$ , which corresponds to  $A_m \simeq 0.8$ .

## Author details

Yoshito Shuto  
Ofra Project, Iruma, Japan

\*Address all correspondence to: [ofra@tuba.ocn.ne.jp](mailto:ofra@tuba.ocn.ne.jp)

## IntechOpen

© 2018 The Author(s). Licensee IntechOpen. This chapter is distributed under the terms of the Creative Commons Attribution License (<http://creativecommons.org/licenses/by/3.0/>), which permits unrestricted use, distribution, and reproduction in any medium, provided the original work is properly cited. 

## References

- [1] Sano A, Kobayashi T, Yamanaka S, Matsuura A, Kawakami H, Miyamoto Y, et al. 102.3-Tb/s (224 x 548-Gb/s) C- and extended L-band all-Raman transmission over 240 km using PDM-64QAM single carrier FDM with digital pilot tone. *Optical Fiber Communication Conference Exhibition/ National Fiber Optic Engineers Conference 2012 (OFC/NFOEC2012); PDP5C.3*
- [2] Nakazawa M. Evolution of EDFA from single-core to multi-core and related recent progress in optical communication. *Optical Review*. 2014; **21**(6):862-874
- [3] Morioka T. New generation optical infrastructure technologies: "EXAT initiative" toward 2020 and beyond. *OptoElectronics and Communications Conference 2009 (OECC 2009); FT4*
- [4] Richardson DJ, Fini JM, Nelson LE. Space-division multiplexing in optical fibres. *Nature Photonics*. 2013; **7**:354-362
- [5] Takara H, Asano A, Kobayashi T, Kubota H, Kawakami H, Matsuura A, et al. 1.01-Pb/s (12 SDM/222 WDM/456 Gb/s) crosstalk-managed transmission with 91.4-b/s/Hz aggregate spectral efficiency. *European Conference on Optical Communication 2012 (ECOC2012); Th.3.C.1*
- [6] Kashyap R, Blow KJ. Observation of catastrophic self-propelled self-focusing in optical fibres. *Electronics Letters*. 1988; **24**(1):47-49
- [7] Kashyap R. Self-propelled self-focusing damage in optical fibres. *Proceedings of Xth International Conference on Lasers*; 1988. pp. 859-866
- [8] Hand DP, Russell PSJ. Solitary thermal shock waves and optical damage in optical fibers: The fiber fuse. *Optics Letters*. 1988; **13**(9):767-769
- [9] Hand DP, Russell PSJ. Soliton-like thermal shock-waves in optical fibers: Origin of periodic damage tracks. *European Conference on Optical Communications*. 1988:111-114
- [10] André P, Rocha A, Domingues F, Facão M. Thermal effects in optical fibres. In: Bernardes MAD, editor. *Developments in Heat Transfer*. Rijeka, Croatia: InTech; 2011
- [11] Todoroki S. Fiber fuse propagation behavior. In: Moh Y, Harun SW, Arof H, editors. *Selected Topics on Optical Fiber Technology*. Rijeka, Croatia: InTech; 2012
- [12] Kashyap R. The fiber fuse—From a curious effect to a critical issue: A 25th year retrospective. *Optics Express*. 2013; **21**(5):6422-6441
- [13] Todoroki S. *Fiber Fuse: Light-Induced Continuous Breakdown of Silica Glass Optical Fiber*. NIMS Monographs. Tokyo: Springer; 2014
- [14] Shuto Y. Simulation of fiber fuse phenomenon in single-mode optical fibers. In: Yasin M, Arof H, Harun SW, editors. *Advances in Optical Fiber Technology*. Rijeka, Croatia: InTech; 2014
- [15] Kashyap R. High average power effects in optical fibres and devices. In: Limberger HG, Matthewson MJ, editors. *Proceedings of Society of Photo-Optical Instrumentation Engineers*. 2003. Vol. 4940. pp. 108-117
- [16] Todoroki S. Quantitative evaluation of fiber fuse initiation probability in typical single-mode fibers. *Optical Fiber Communication Conference*; 2015 (OFC2015); W2A.33
- [17] Todoroki S. Quantitative evaluation of fiber fuse initiation with exposure to arc discharge provided by a fusion

- splicer. *Scientific Reports*. 2016;**6**:25366-1-25366-6
- [18] Dianov EM, Bufetov IA, Frolov AA. Destruction of silica fiber cladding by the fuse effect. *Optics Letters*. 2004; **29**(16):1852-1854
- [19] Kurokawa K, Hanzawa N. Fiber fuse propagation and its suppression in hole assisted fibers. *IEICE Transactions on Communications*. 2011;**E94-B**(2):384-391
- [20] Dianov EM, Mashinsky VM, Myzina VA, Sidorin YS, Streltsov AM, Chickolini AV. Change of refractive index profile in the process of laser-induced fibre damage. *Soviet Lightwave Commun*. 1992;**2**:293-299
- [21] Davis DD, Mettler SC, DiGiovanni DJ. Experimental data on the fiber fuse. In: Bennett HE, Guenther AH, Kozlowski MR, Newnam BE, Soileau MJ, editors. *Proceedings of Society of Photo-Optical Instrumental Engineers*. 1995;**2714**:202-210
- [22] Davis DD, Mettler SC, DiGiovanni DJ. A comparative evaluation of fiber fuse models. In: Bennett HE, Guenther AH, Kozlowski MR, Newnam BE, Soileau MJ, editors. *Proceedings of Society of Photo-Optical Instrumental Engineers*. 1966;**2966**:592-606
- [23] Todoroki S. Origin of periodic void formation during fiber fuse. *Optics Express*. 2005;**13**(17):6381-6389
- [24] Todoroki S. In situ observation of modulated light emission of fiber fuse synchronized with void train over hetero-core splice point. *PLoS One*. 2008;**3**(9):e3276-1-4
- [25] Domingues F, Frias AR, Antunes P, Sousa AOP, Ferreira RAS, André PS. Observation of fuse effect discharge zone nonlinear velocity regime in erbium-doped fibres. *Electronics Letters*. 2012;**48**(20):1295-1296
- [26] S. Todoroki. Fiber fuse propagation modes in typical single-mode fibers. *Optical Fiber Communication Conference 2013 (OFC2013)*; JW2A.11
- [27] Antunes PFC, Domingues MFF, Alberto NJ, André PS. Optical fiber microcavity strain sensors produced by the catastrophic fuse effect. *IEEE Photonics Technology Letters*. 2014; **26**(1):78-81
- [28] Lin G, Baiad MD, Gagne M, Liu W, Kashyap R. Harnessing the fiber fuse for sensing applications. *Optics Express*. 2014;**22**(8):8962-8969
- [29] Domingues MFF, Paixão TB, Mesquita EFT, Alberto N, Frias AR, Ferreira RAS, et al. Liquid hydrostatic pressure optical sensor based on micro-cavity produced by the catastrophic fuse effect. *IEEE Sensors Journal*. 2015; **15**(10):5654-5658
- [30] Bufetov IA, Frolov AA, Dianov EM, Frotov VE, Efremov VP. Dynamics of fiber fuse propagation. *Optical Fiber Communication Conference Exhibition/ National Fiber Optical Engineering Conference 2005 (OFC/NFOEC2005)*; OThQ7
- [31] Dianov EM, Frotov VE, Bufetov IA, Efremov VP, Rakitin AE, Melkumov MA, et al. High-speed photography, spectra, and temperature of optical discharge in silica-based fibers. *IEEE Photonics Technology Letters*. 2006; **18**(6):752-754
- [32] Atkins RM, Simpkins PG, Yabon AD. Track of a fiber fuse: A Rayleigh instability in optical waveguides. *Optics Letters*. 2003;**28**(12):974-976
- [33] Yakovlenko SI. Plasma behind the front of a damage wave and the mechanism of laser-induced production of a chain of caverns in an optical fibre. *Quantum Electronics*. 2004;**34**(8):765-770



- [34] Yakovlenko SI. Mechanism for the void formation in the bright spot of a fiber fuse. *Laser Physics*. 2006;**16**(3): 474-476
- [35] Kawabe T, Kawai Y, Takayama K. Interaction between high frequency oscillations and low frequency oscillations in beam-plasma system. *Journal of the Physical Society of Japan*. 1967;**23**:1430-1431
- [36] Abrams RH Jr, Yadlowsky EJ, Lashinsky H. Periodic pulling and turbulence in a bounded plasma. *Physical Review Letters*. 1969;**22**(7): 275-278
- [37] Stix TH. Finite-amplitude collisional drift waves. *Physics of Fluids*. 1969; **12**(3):627-639
- [38] Keen BE, Fletcher WHW. Suppression and enhancement of an ion-sound instability by nonlinear resonance effects in a plasma. *Physical Review Letters*. 1969;**23**(14):760-763
- [39] Keen BE, Fletcher WHW. Suppression of a plasma instability by the method of asynchronous quenching. *Physical Review Letters*. 1970;**24**(4): 130-134
- [40] Keen BE. Interpretation of experiments on feedback control of a "drift-type" instability. *Physical Review Letters*. 1970;**24**(6):259-262
- [41] Shut'ko AV. Finite amplitude ion acoustic waves in an unstable plasma. *Soviet Physics-JETP*. 1970;**30**(2): 248-251
- [42] Nakamura Y. Suppression of two-stream instability by beam modulation. *Journal of the Physical Society of Japan*. 1979;**28**(5):1315-1321
- [43] Keen BE, Fletcher WHW. Remote feedback stabilization of the ion-sound instability by a modulated source at the electron-cyclotron resonance frequency. *Physical Review Letters*. 1970;**25**(6): 350-353
- [44] Keen BE, Fletcher WHW. Measurement of growth rate, non-linear saturation coefficients, and mode-mode coupling coefficients of a 'Van der Pol' plasma instability. *Journal of Physics D*. 1970;**3**:1868-1885
- [45] Nakamura Y. Suppression and excitation of electron oscillation in a beam-plasma system. *Journal of the Physical Society of Japan*. 1971;**31**(1): 273-279
- [46] Keen BE, Fletcher WHW. Nonlinear plasma instability effects for subharmonic and harmonic forcing oscillations. *Journal of Physics A*. 1972;**5**: 152-165
- [47] Boswell RW, Christiansen PJ, Salter CR. Nonlinear effects in an r.f. plasma. *Physics Letters A*. 1972;**38**(2):67-68
- [48] Tavzes R, Cercek M. Frequency entrainment of a drift instability by nonlinear effects in a plasma. *Physics Letters A*. 1973;**43**(2):99-100
- [49] DeNeef P, Lashinsky H. Van der Pol model for unstable wave on a beam-plasma system. *Physical Review Letters*. 1973;**31**(17):1039-1041
- [50] Keen BE, Fletcher WHW. The ion-sound instability and its associated multi-mode phenomena. *Journal of Physics D*. 1973;**6**:1684-1698
- [51] Michelsen P, Pecseli HL, Rasmussen JJ, Schrittwieser R. The current-driven, ion-acoustic instability in a collisionless plasma. *Plasma Physics*. 1979;**21**:61-73
- [52] Ohno N, Tanaka M, Komori A, Kawai Y. Chaotic behavior of current-carrying plasmas in external periodic oscillations. *Journal of the Physical Society of Japan*. 1989;**58**(1):28-31

- [53] Buragohain A, Chutia J, Nakamura Y. Mode suppression and period-doubling cascade in a double-plasma device. *Physics Letters A*. 1992;**163**: 425-428
- [54] Gyergyek T, Cercek M, Jelic N, Stanojevic M. Mode suppression of a two-dimensional potential relaxation instability in a weakly magnetized discharge plasma. *Physics Letters A*. 1993;**176**(1):54-60
- [55] Klinger T, Piel A, Seddighi F, Wilke C. Van der Pol dynamics of ionization plasma. *Physics Letters A*. 1993;**182**(2-3):312-318
- [56] van der Pol B. The nonlinear theory of electric oscillations. *Proc. Inst. Radio Engineering*. 1934;**22**(9): 1051-1086
- [57] Shuto Y. Heat conduction modeling of fiber fuse in single-mode optical fibers. *Journal of Photonics*. 2014;**2014**: Article ID 645207-1-21
- [58] Shuto Y, Yanagi S, Asakawa S, Kobayashi M, Nagase R. Fiber fuse phenomenon in step-index single-mode optical fibers. *IEEE Journal of Quantum Electronics*. 2004;**40**(8):1113-1121
- [59] Bumarín ED, Yakovlenko SI. Temperature distribution in the bright spot of the optical discharge in an optical fiber. *Laser Physics*. 2006;**16**(8): 1235-1241
- [60] Facão M, Rocha A, André P. Traveling solution of the fuse effect in optical fibers. *IEEE/OSA Journal Lightwave Technology*. 2011;**29**(1): 109-114
- [61] Todoroki S. Threshold power reduction of fiber fuse propagation through a white tight-buffered single-mode optical fiber. *IEICE Electronics Express*. 2011;**8**(23): 1978-1982
- [62] Boyd RW. *Nonlinear Optics*. Chap. 1. New York: Academic Press, Inc.; 1992
- [63] Okuyama A. *Material Dynamics (Augmented Version)*. Chap. 5. Tokyo: Corona-sha; 1958
- [64] Yokobori T. *An Interdisciplinary Approach to Fracture and Strength of Solids*. Chap. 1. Amsterdam: Gordon & Breach Publishers; 1968
- [65] Schick HL. A thermodynamic analysis of the high-temperature vaporization properties of silica. *Chemical Reviews*. 1960;**60**:331-362
- [66] Shuto Y. Evaluation of high-temperature absorption coefficients of ionized gas plasmas on optical fibers. *IEEE Photonics Technology Letters*. 2010;**22**(3):134-136
- [67] JANAF. *Thermochemical Tables*. 2nd ed. U.S. Department of Commerce and National Bureau of Standards; 1971
- [68] Saha MN. Ionization in solar chromosphere. *Philosophical Magazine*. 1920;**40**(238):472-488
- [69] Kittel C. *Introduction to Solid State Physics*. Chap. 3. 7th ed. New York: John Wiley & Sons, Inc.; 1996
- [70] Castellan GW. *Physical Chemistry*. Chap. 33. 3rd ed. Boston: Addison-Wesley Publishing Co., Inc.; 1983
- [71] *Chemical Data Book*. Chap. 9. 3th ed. Tokyo: Chemical Society of Japan; 1984
- [72] Shuto Y. End face damage and fiber fuse phenomena in single-mode fiber-optic connectors. *Journal of Photonics*. 2016;**2016**: Article ID 2781392-1-11
- [73] Moore WJ. *Physical Chemistry*. Chap. 4. 4th ed. Princeton: Prentice Hall, Inc; 1972

[74] Brennen CE. Cavitation and Bubble Dynamics. Chap. 1. New York: Cambridge University Press; 2014

[75] Schottky W. Diffusionstheorie der positiven Säule. Physikalische Zeitschrift. 1924;**25**:635-640

[76] Allis WP, Rose DJ. The transition from free to ambipolar diffusion. Physics Review. 1954;**93**(1):84-93

[77] Phelps AV. The diffusion of charged particles in collisional plasmas: Free and ambipolar diffusion at low and moderate pressures. Journal of Research of the National Institute of Standards and Technology. 1990;**95**(4):407-431

[78] Ohtori S, Sekiguchi T, Kawano T. Theory of Discharged Gases. Chap. 2. Tokyo: Ohmsha Inc.; 1969

[79] Israelachvili JN. Intermolecular and Surface Forces. Chap. 12. 2nd ed. London: Academic Press, Ltd.; 1992

[80] Kawakubo T, Kabashima S. Stochastic processes in self-excited oscillation. Journal of the Physical Society of Japan. 1974;**37**(5):1199-1203